Plasmonic Sensing of Oncoproteins without Resonance Shift Using 3D Periodic Nanocavity in Nanocup Arrays

*Abid Ameen, Lisa P. Hackett, Sujin Seo, Faiza Khawar Dar, Manas R. Gartia, Lynford L. Goddard, and Gang Logan Liu**

A sensor design and sensing method based on plasmonic–photonic interactions that occur when a nanocavity array is embedded in a 3D tapered nanocup plasmonic substrate are reported. This device enables highly sensitive detection of refractive index changes based on changes to the transmission peak intensity without shift in the resonance wavelength. Unlike conventional plasmonic sensors, there is a consistent and selective change in the transmission intensity at the resonance peak wavelength with no spectral shift. In addition, there are wavelength ranges that show no intensity change, which can be used as reference regions. The fabrication and characterization of the plasmonic nanocavity sensor are described and also advanced biosensing is demonstrated. Simulations are carried out to better understand the plasmon–photonic coupling mechanism. This nanocavity plasmonic sensor design has a limit of detection of 1 ng mL^{-1} (5×10^{-12} M) for the cancer biomarker carcinoembryonic antigen (CEA), which is a significant improvement over current surface plasmon resonance systems, and a dynamic range that is clinically relevant for human CEA levels.

1. Introduction

Label-free sensors for the detection of low concentrations of biomolecules, such as cancer biomarkers, are highly sought after for applications including drug discovery research and point-of-care diagnostics. Optical devices such as the photonic crystal,[1] ring resonator,[2] interferometer,[3] and surface plasmon resonance (SPR) sensor,[4] are promising alternatives to the traditional enzyme-linked immunosorbent assay techniques due to their sensitive detection.[5] However, bulky external optical setups with precise alignment are required, which limits widespread applications. Alternatively, plasmonic sensors based on extraordinary optical transmission (EOT)[6] allow the excitation of surface plasmons with an incoherent light source and the detection with a portable spectrometer; however, the sensitivity of these devices is an order of magnitude lower than conventional SPR sensors.[7]

Here, we report a new nanoplasmonic resonance sensor design that shows a unique interactive plasmonic–photonic resonance effect: only resonance peak intensity variation, not a plasmon resonance wavelength shift, is observed in the far field as a function of the optical refractive index (RI) on the superstrate when a periodic plasmonic nanostructure and a multilayer nanocavity are combined. Multilayer plasmonic structures have been investigated for on-chip photonic devices, such as multilayered plasmonic waveguides.[8] Metal–insulator–metal (MIM) surface plasmon waveguides have been studied for refractometric detection.[9] In addition, the localized surface plasmon resonance (LSPR) effect has been used with multilayered geometries to increase light-induced catalytic activity of materials such as palladium.[10] The study of dielectric films and MIM structures combined with an EOT substrate has been reported previously.[11] However, these prior works focused on surface enhanced Raman spectroscopy applications or on the plasmon resonance peak shift of nanohole arrays and the sensitivity of these structures to superstrate RI changes was lower than conventional EOT devices.

The new hybrid nanoplasmonic–nanocavity sensor that we utilize here is based on a 3D plasmonic nanocup resonator structure, which consists of a nanostructured polymer substrate with a deposited gold (Au) layer.[12] To form a nanocavity

Dr. A. Ameen, Dr. S. Seo
Department of Materials Science and Engineering
Micro and Nanotechnology Laboratory
University of Illinois at Urbana-Champaign
Urbana, IL 61801, USA

L. P. Hackett, Prof. L. L. Goddard, Prof. G. L. Liu
Department of Electrical and Computer Engineering
Micro and Nanotechnology Laboratory
University of Illinois at Urbana-Champaign
Urbana, IL 61801, USA
E-mail: loganliu@illinois.edu

DOI: 10.1002/adom.201601051

Dr. F. K. Dar
Department of Bioengineering
University of Illinois at Urbana-Champaign
Urbana, IL 61801, USA

Prof. M. R. Gartia
Department of Mechanical and Industrial Engineering
Louisiana State University
Baton Rouge, LA 70803, USA

Prof. G. L. Liu
School of Life Science and Technology
Huazhong University of Science and Technology
Wuhan, Hubei 430074, China

© 2017 WILEY-VCH Verlag GmbH & Co. KGaA, Weinheim

embedded in the plasmonic nanocup array, we deposit a CdS or SiO_2 layer on the first Au layer followed by a second Au layer. The CdS layer is chosen due to its high RI and low extinction coefficient (k) in the visible light range, while the Au layers provide strong confinement of the electromagnetic field on the nanoscale. Here we will refer to this distinct nanoplasmonic–nanocavity device as a multilayer nano Lycurgus cup array (ML-nanoLCA), due to the similar optical properties of the underlying nanocup structure to the Lycrugus cup developed by the Ancient Romans. We have found that by the addition of a nanostructured cavity array on a high-performing conventional nanoplasmonic sensor, entirely new optical and spectral properties are observed. In particular, for the ML-nanoLCA, an increase in RI of the superstrate results in an increase in the transmission intensity or equivalently resonance extraction at the plasmon resonance wavelength, but no shift in the peak wavelength position. Detection is achieved by monitoring the change in transmitted intensity at the resonance wavelength. In addition, our sensor contains a wavelength region where no intensity change occurs with varying RI. Other groups have reported intensity-based detection using EOT devices where molecular binding events typically result in a decrease in transmission intensity (increase in absorbance).[13] However, complex experimental setups and substantial postprocessing of the data are required to obtain consistent results since these spectral features also contain shifts and no reference regions. Therefore, we introduce a new plasmonic sensing model where RI changes result in no peak wavelength shift, but can be detected with a high sensitivity using the peak intensity variation.

In this work, we describe the fabrication, characterization, and principle of operation of the ML-nanoLCA device along with ultrasensitive label-free biomolecular detection. The device design is further optimized by tuning the layer thicknesses for a better sensitivity and then applied to detect the cancer biomarker carcinoembryonic antigen (CEA). CEA is produced during fetal development and its production terminates before birth. The normal level of CEA for a healthy person is around 3–5 ng mL^{-1}.[14] However, there is a considerable increase (>10 ng mL^{-1}) in its concentration for people with conditions like lung cancer,[15] colorectal carcinoma,[16] and breast carcinoma.[17] We report that the ML-nanoLCA achieves a label-free limit of detection (LOD) of 1 ng mL^{-1} (5×10^{-12} M) for CEA simply by monitoring the peak intensity change. In this work, the LOD is defined by the lowest detectable concentration of CEA for the values tested. Therefore, the actual LOD of this device may be lower than the experimental value reported here. This sensing performance of the ML-nanoLCA is outstanding compared to that of current SPR systems. A LOD of 100 ng mL^{-1} for CEA was reported when using a commercially available SPR system and a secondary antibody label was required to reduce the LOD to 3 ng mL^{-1}.[18]

The optical properties and biosensing results for our nanocavity plasmon resonance sensor presented in this work have important implications for future point-of-care plasmon resonance sensing systems. This device only requires normal incident light for the RI detection and the results are independent of the polarization. The spectral features suggest that illumination and detection can be achieved using only an incoherent light source with a narrowband filter or a light-emitting diode (LED) and photodetector. Therefore, no spectrometer or other specialized equipment is required. In addition, since the intensity changes within a fixed wavelength range and there are spectral regions where no intensity change occurs, this device has a high potential to be self-referencing if the optical excitation and detection are designed properly. The ability for the device to act as its own reference sample has particular importance for intensity-based measurements where sample-to-sample variations can be difficult to control in applications done outside of a controlled laboratory setting. For example, reference regions can be used to detect small changes in light source intensity that is not due to any RI change. We anticipate that these advantages of our device will make feasible the development of a portable point-of-care biosensor for early detection of disease biomarkers.

2. Results and Discussion

2.1. Fabrication and Characterization of the ML-NanoLCA Sensor

The new design of an intensity-based refractometric sensor is fabricated by combining a MIM multilayer structure and a 3D nanocup array. **Figure 1**a shows a schematic of the ML-nanoLCA, which consists of a polymeric (i.e., NOA-61 UV-curable polymer) nanocup array structure and the deposited MIM of 90 nm Au, 40 nm CdS, and 50 nm Au. The multilayer structure is shown in Figure 1b with a cross-sectional view taken by a focused ion beam (FIB). All three stacked layers of the ML-nanoLCA device are clearly distinguishable. Figure 1c shows a scanning electron microscope (SEM) image of the top view of the device and Figure 1d shows a camera image taken under ambient illumination. The surface morphology of the device, obtained by an atomic force microscope (AFM) scan, is shown in Figure 1e with a graph that shows the approximate depth of the periodic hole structure to be 300 nm. The spectra of the device with only the first Au layer and no cavity structure in air (RI = 1), water (RI = 1.33), and isopropyl alcohol (IPA) (RI = 1.37) are shown in Figure 1f. Without the cavity structure, a red shift in the resonance wavelength is observed when the RI of the superstrate increases. However, as shown in Figure 1g, once the multilayer structure is introduced, an increase in RI causes an increase in intensity, but no detectable shift for the prominent peak at 695 nm.

2.2. Sensitivity and Optical Properties

In order to assess the sensitivity of the ML-nanoLCA device, different concentrations of sucrose solutions (from 0% (w/v) to 60% in Milli-Q water) were added onto the superstrate. This change in concentration of the sucrose corresponds to a bulk RI change from 1.33 to 1.44. With increasing RI, there was an increase in the intensity of the resonance peak in the transmission spectrum, but no spectral shift, as shown in **Figure 2**a. In order to identify the effect of the material properties of the sandwiched insulator in the MIM structure, the layer of CdS

© 2017 WILEY-VCH Verlag GmbH & Co. KGaA, Weinheim

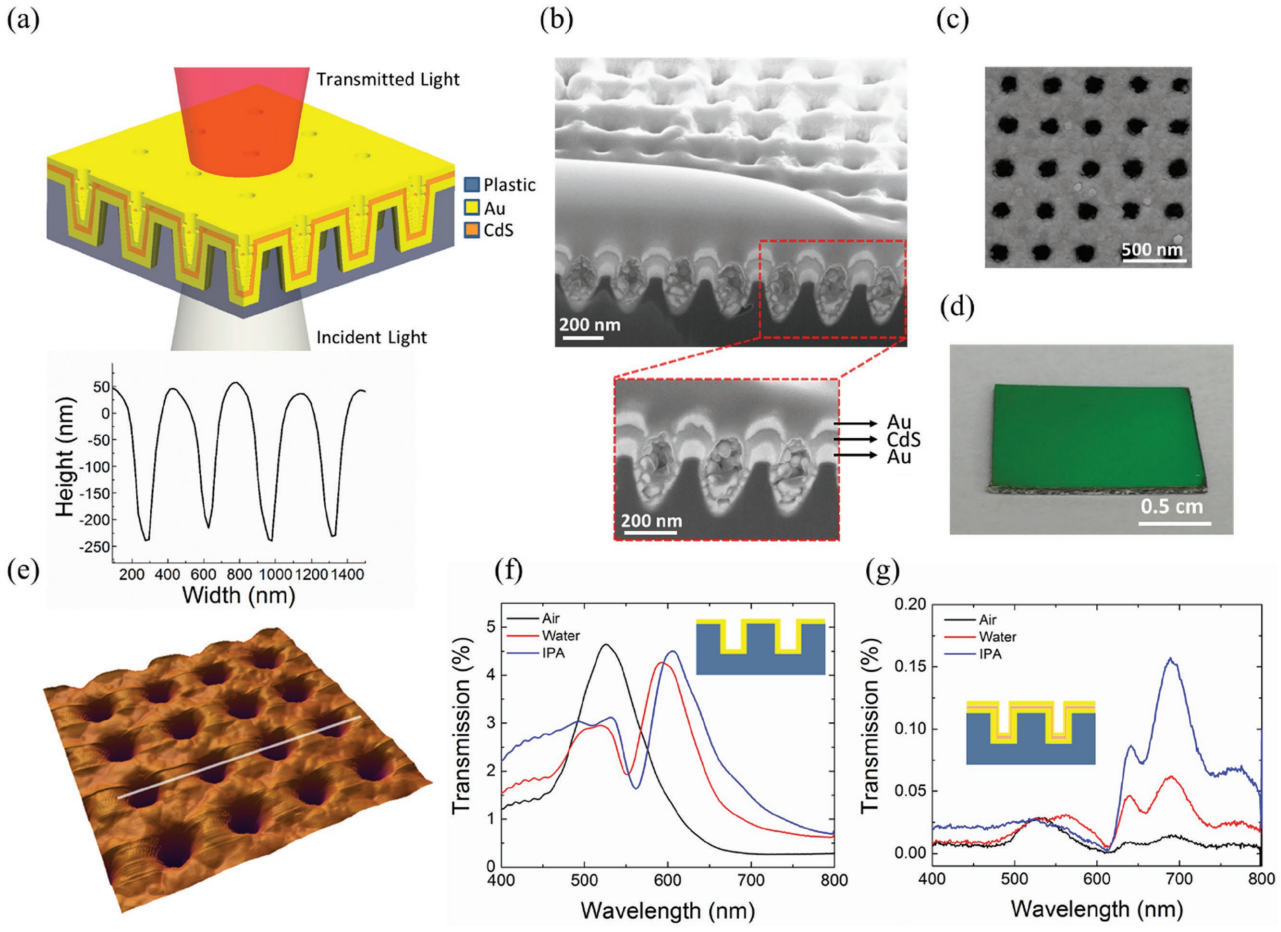

Figure 1. a) Schematic illustration of the ML-nanoLCA showing the multilayer structure and direction of illumination. b) Cross-sectional view of the device taken with a FIB with an expanded view of three nanocups. c) SEM image of the top view of the device. d) Camera image of the ML-nanoLCA taken under ambient illumination. e) AFM scan of the device to show the surface morphology. The graph on the top shows the depth of the periodic hole structure. A comparison of the transmission spectra f) for the device with only the first Au layer and g) for the ML-nanoLCA device with air (RI = 1), water (RI = 1.33), and IPA (RI = 1.37) as the superstrate materials. An increase in the RI of the superstrate causes a red shift in the resonance peak for the case with no cavity structure and an increase in intensity with no detectable shift in the resonance peak for the ML-nanoLCA.

(RI ≈ 2.5) was replaced by a 40 nm layer of SiO_2 (RI ≈ 1.45). This modified MIM structure also showed the transmission intensity consistently increasing with an increase in the RI of the superstrate as shown in Figure 2b.

To verify this experimental finding, a 3D finite-difference time-domain (3D-FDTD) study was carried out and the transmission spectra were collected for both structures (one MIM structure with CdS and the other with SiO_2) with increasing RI of the superstrate as shown in Figure 2c,d. The simulation results agree well with the experimental spectra. Spectral differences between the experimental results and simulation may be due to various factors, such as the wettability of the device. Although the SiO_2 layer shows a similar transmission intensity trend to the CdS layer, the increase in the transmission intensity is relatively small when compared to the CdS device as shown in Figure 2e. The sensitivity of the devices is calculated by the relative change in the transmission intensity (T) at the resonance wavelength per RI unit (RIU) such that the final unit for sensitivity is $\Delta\%T$/RIU. The calculated sensitivity of the ML-nanoLCA device with CdS is 660 $\Delta\%T$/RIU at $\lambda = 695$ nm while the calculated sensitivity for the device with SiO_2 is 340 $\Delta\%T$/RIU at $\lambda = 672$ nm. Therefore, by using CdS instead of SiO_2 as the cavity layer, the sensitivity is approximately doubled. The simulated transmission spectra for additional cavity materials are shown in Figure S1 (Supporting Information).

The electric field distribution for the ML-nanoLCA was obtained by the 3D-FDTD simulations. **Figure 3**a shows the electric field distribution for the cross section of the nanocup at the resonance peak wavelength with a superstrate RI of 1.33. Due to the higher RI of the cavity layer compared to the superstrate, the electric field is confined at the interface between the bottom Au and CdS layer. Furthermore, the top Au layer helps confine the generated mode between the two Au layers, forming a cavity. As the RI of the superstrate is increased, as shown in Figure 3b,c, the magnitude of the electric field is decreased at the interface between the CdS and the bottom Au layer, but is increased in the top Au layer, which enables the outcoupling to the top Au layer; hence, the overall transmission intensity is enhanced.

© 2017 WILEY-VCH Verlag GmbH & Co. KGaA, Weinheim

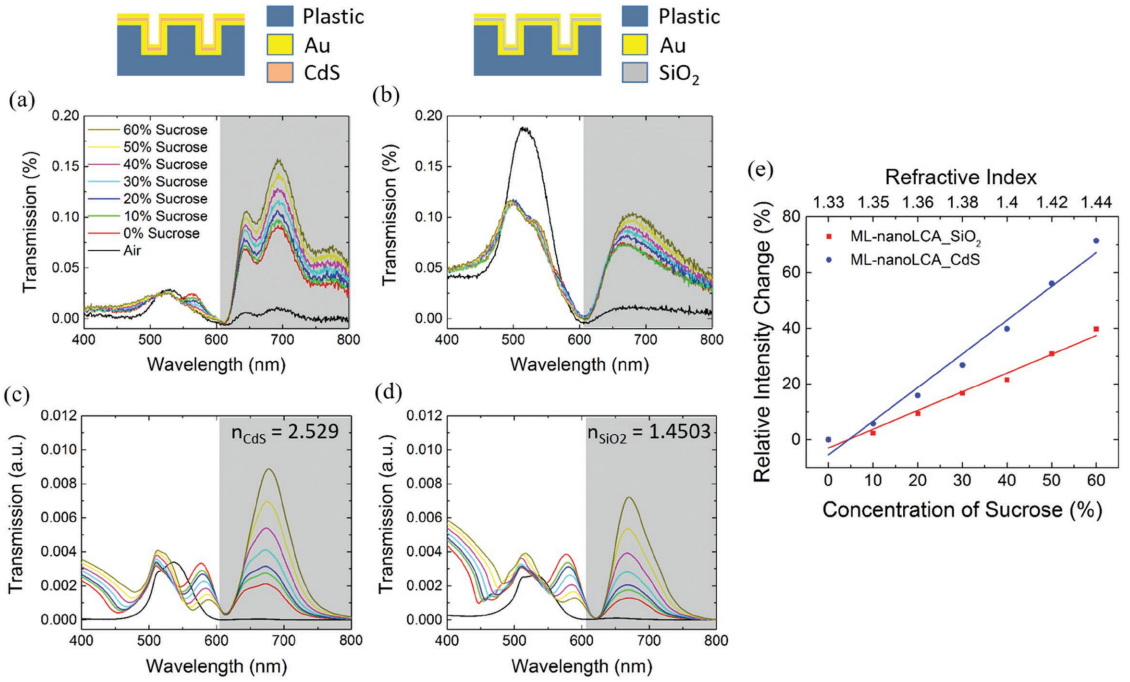

Figure 2. Experimental transmission spectra for a) CdS and b) SiO_2 for solutions with increasing concentrations of sucrose (from 0% to 60%). Theoretical spectral response to the increasing sucrose concentrations for c) CdS and d) SiO_2 computed by 3D-FDTD simulations of the ML-nanoLCA structure. e) Graph comparing the relative intensity change of the ML-nanoLCA device between CdS and SiO_2 with respect to the increasing concentrations of the sucrose solution and increasing RI.

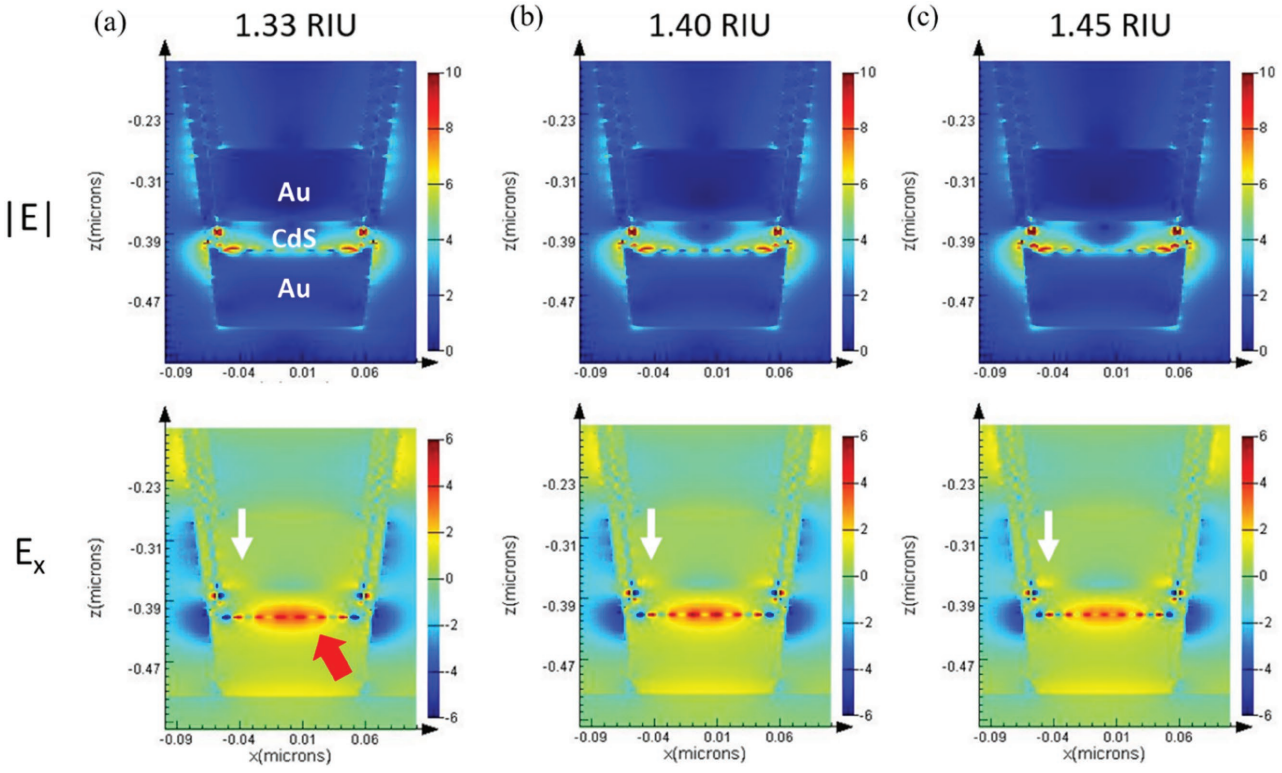

Figure 3. Plots of the absolute electric field ($|E|$) and the electric field in *x*-direction (E_x) in the cross-sectional view of the ML-nanoLCA at the resonance wavelength when the RI is a) 1.33, b) 1.40, and e) 1.45. The red arrow indicates the confined mode at the Au–CdS interface while the white arrow indicates the outcoupling of the mode to the top Au layer as the RI of the superstrate is increased.

© 2017 WILEY-VCH Verlag GmbH & Co. KGaA, Weinheim

2.3. DNA Hybridization and Biotin–Streptavidin Biosensing

To demonstrate label-free detection of biomolecular interaction on the surface of the ML-nanoLCA, we detected DNA hybridization and biotin–streptavidin binding. For the ssDNA hybridization process, the ML-nanoLCA device was first immersed in a 10×10^{-6} M single-stranded DNA (ssDNA) probe solution (DNA-1), which is modified by a thiol group at one end of the DNAs to immobilize them onto the top Au layer. The device was then immersed into a 1×10^{-6} M blocking solution (6-mercapto-1-hexanol (MCH)) followed by immersion in 1×10^{-6} M DNA-2 (3′ complimentary base pair) and the hybridization reaction occurred. **Figure 4**a shows the transmission spectra measured after each step with an inset schematic of the process. The transmission spectra are zoomed in and replotted in Figure 4b to highlight the intensity change at the peak wavelength. The average intensity values at each step for two trials are shown in the bar graph in Figure 4c with error bars representing the standard deviation. There is an increase in the transmission intensity from 0.076 ± 0.006% to 0.191 ± 0.005% due to surface binding of DNA-1 and a small decrease in intensity to 0.189 ± 0.006% following MCH incubation. The hybridization reaction is detected by an increase in transmission intensity to 0.203 ± 0.007% at the resonance wavelength following immersion in the DNA-2 solution. It is important to note the performance of this plasmonic nanocavity device in terms of signal-to-noise ratio. We determined the noise in the measured intensity for a single sample to be 0.0008% based on the standard deviation of the signal in the flat spectral region from 400 to 425 nm. Here we see that the starting signal in terms of the intensity value is 0.076% and therefore the signal-to-noise ratio will always be greater than 95. If we define the signal to be the lowest detectable relative intensity change, which for this device is 1%, then the signal-to-noise ratio will always be greater than 1250.

The ML-nanoLCA was also evaluated for detection of high affinity ($K_a \approx 10^{15}$ M^{-1}) streptavidin–biotin binding. The surface of the sensor was functionalized with biotin and then immersed in a 1×10^{-3} M MCH blocking solution followed by 1 µg mL^{-1} (18.9×10^{-9} M) streptavidin. The transmission spectra for each step with a schematic of the process are shown in Figure 4d and the change in intensity is shown in Figure 4e. As expected, immobilization of the thiolated biotin resulted in an increase in the transmission intensity at the peak wavelength, immersion in the MCH solution resulted in a small decrease in the transmission intensity, and binding of streptavidin to the surface resulted in a transmission intensity increase. The transmission measurement was performed over time to monitor streptavidin binding as shown in Figure 4f.

2.4. Carcinoembryonic Antigen Detection

The detection of DNA hybridization and streptavidin–biotin binding show that the ML-nanoLCA is a good refractometer for detecting small RI changes at the Au–superstrate interface due to molecules or proteins binding on the device surface. This

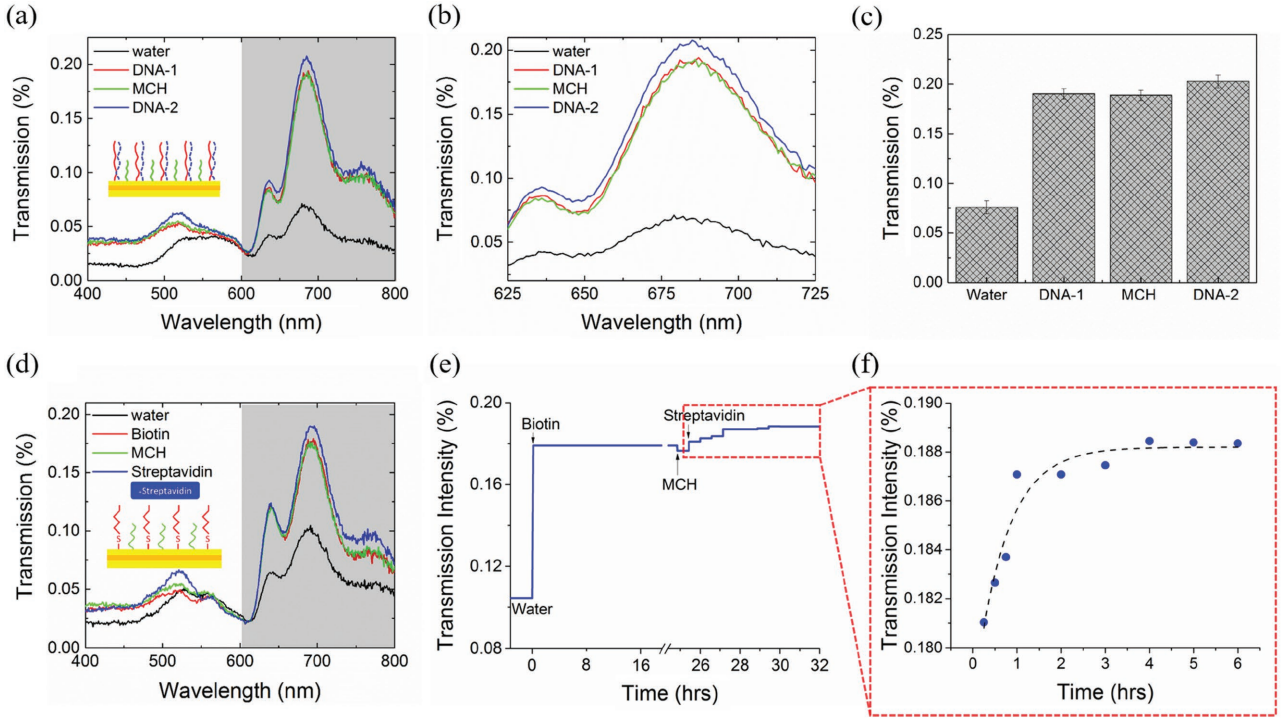

Figure 4. a) Transmission spectra of the device following each ssDNA hybridization step with a schematic shown in the inset. b) Zoomed-in replotting of the transmission spectra to show the change in intensity occurring at the plasmon resonance wavelength. c) Bar graph of the average intensity values for two trials with error bars showing the standard deviation. d) Transmission spectra of the device following each biotin–streptavidin conjugation with a schematic shown in the inset. e) Binding of streptavidin to biotin with respect to time detected by the change of the peak transmission intensity of the device. f) Plot of percent transmission at the resonance peak wavelength with respect to time during streptavidin binding.

© 2017 WILEY-VCH Verlag GmbH & Co. KGaA, Weinheim

was accomplished by simply monitoring the intensity change at the transmission peak. However, the relative percent intensity increase was only 7.7% for detecting a streptavidin concentration of 1 μg mL^{-1} (18.9×10^{-9} M). In order to detect a clinically relevant concentration of CEA for a diagnosis, it is required to have a LOD of at least 3 ng mL^{-1} and therefore further optimization of the device with a better sensitivity was needed. We modified the cavity structure by changing the thickness of each MIM layer for higher sensitivity. The top Au layer was decreased by a factor of two from 50 to 25 nm in order to reduce loss in the metal and increase the overall transmission through the device. In addition, the CdS cavity layer thickness was increased by a factor of two from 40 to 80 nm in order to increase the electric field confinement in the cavity. These modifications to the cavity structure also red shifted the transmission peak from 695 to 765 nm.

A schematic of the surface functionalization of the ML-nanoLCA for CEA detection is shown in **Figure 5**a. The device was immersed in a 10×10^{-3} M 11-mercaptuoudecanoic acid (MUA) solution, which formed a self-assembled monolayer, and the CEA antibody (30 μg mL^{-1}) was then covalently bound to the MUA by 1-ethyl-3-(3-dimethylaminopropyl)carbodiimide (EDC) and *N*-hydroxysuccinimide (NHS) coupling. The device was then incubated in a bovine serum albumin (BSA) blocking solution followed by the incubation in an ethanolamine solution, which reacts with any remaining NHS. Finally, the ML-nanoLCA devices were incubated in different concentrations of CEA in phosphate-buffered saline (PBS) solutions from 0.1 ng mL^{-1} to 1 μg mL^{-1} with one replicate for each concentration. The spectral measurements for the ML-nanoLCA were all taken in water. A vehicle control (PBS containing no CEA) was also used in addition to an antibody control where the nonspecific binding between 1 μg mL^{-1} of CEA to antimouse IgG was measured. We also prepared devices with only the first Au layer and therefore containing no cavity structure with the same surface functionalization and detected the binding of 1 μg mL^{-1} and 100 ng mL^{-1} CEA along with the controls. When the cavity structure is removed the device operates as a conventional plasmonic sensor and a RI change causes a shift in the SPR wavelength.

The measured LOD for the device without the cavity structure is 1 μg mL^{-1} of CEA where there was a 2 nm red shift in

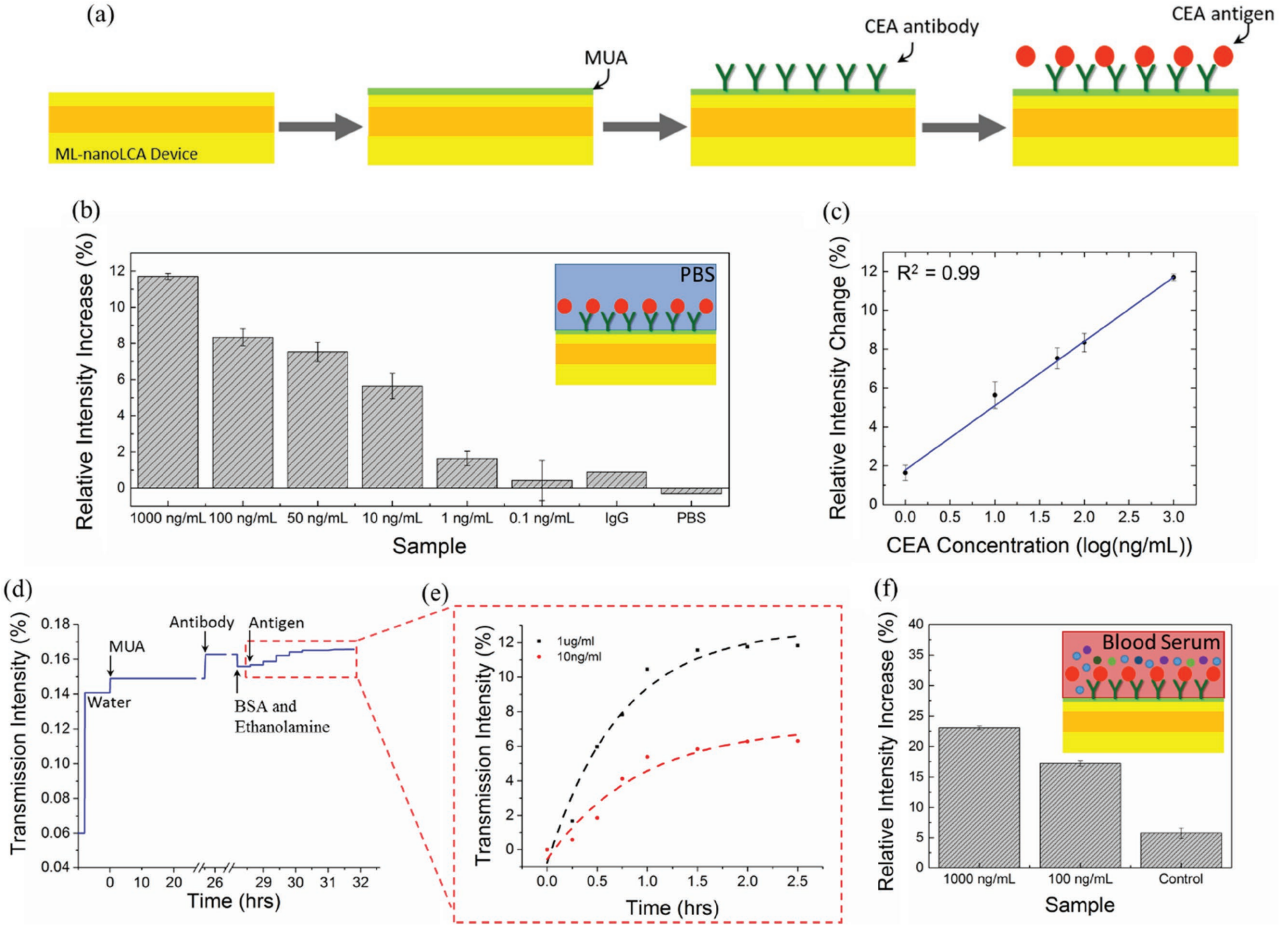

Figure 5. a) Schematic of the surface functionalization for CEA detection. b) Bar graph showing the relative intensity change for six different CEA concentrations along with the antibody control (IgG) and the vehicle control (PBS). c) Plot of the relative intensity change as a function of CEA concentration (log scale). The data were fit to a linear model with good agreement. d) Intensity with respect to time for 10 ng mL^{-1}. e) Plot of percentage transmission intensity change for 1 μg mL^{-1} and 10 ng mL^{-1} CEA binding to the anti-CEA immobilized on the ML-nanoLCA device surface. f) Bar graph showing detection of CEA (1 μg mL^{-1} and 100 ng mL^{-1}) spiked in human blood serum samples compared to the vehicle control of serum only.

© 2017 WILEY-VCH Verlag GmbH & Co. KGaA, Weinheim

the transmission peak position (data shown in Figure S2, Supporting Information). No peak shift was obtained for the controls or the 100 ng mL^{-1} CEA samples. A bar graph showing the relative intensity change for the ML-nanoLCA with the different concentrations of CEA along with the controls is shown in Figure 5b. The LOD for the ML-nanoLCA was 1 ng mL^{-1}. A table in the Supporting Information compares the sensing performance of the ML-nanoLCA to other label-free optical biosensors. There was a small relative intensity change for the antibody control (less than 1%) and a small relative intensity change for the vehicle control (less than 0.5%). Figure 5c shows a plot of the relative intensity change as a function of CEA concentration on a log scale. The data were fit to a linear model and showed good agreement over the three orders of magnitude dynamic range (1–1000 ng mL^{-1}). A plot of the intensity values as a function of time is shown in Figure 5d during the immobilization steps and Figure 5e shows the binding of 1 µg mL^{-1} and 10 ng mL^{-1} CEA. A plot of the sensor response as a function of CEA concentration in $\times 10^{-6}$ M was also fit to the Michaelis–Menten equation (see the Supporting Information and Figure S3, Supporting Information) and the dissociation constant (K_D) of CEA and anti-CEA was experimentally determined to be $K_D = 115 \pm 53 \times 10^{-12}$ M. However, an accurate analysis of surface-binding interactions requires more complicated models, such as the combination of Michaelis–Menten kinetics and Langmuir adsorption models.[19] Here, we show a greatly simplified analysis in order to demonstrate that this device has the potential to determine kinetic parameters like conventional plasmonic sensors. In addition, CEA concentrations of 1 µg mL^{-1} and 100 ng mL^{-1} were spiked in human serum samples and detected with a result that was distinguishable from the vehicle control as shown in Figure 5f.

2.5. Cavity Structure Analysis

The modification to the cavity structure, which enabled a LOD of 1 ng mL^{-1} for CEA detection, is illustrated in **Figure 6**a. By decreasing the top Au layer to 25 nm and increasing the CdS layer to 80 nm the sensitivity was increased from 660 to 1150 Δ%T/RIU. The transmission spectra used to calculate the sensitivity for the modified device are shown in Figure 6b and the plot of the sensitivity is shown in Figure 6c. The effects of the modification were visualized by plotting the electric field distribution in the cavity structure using the transfer matrix method as shown in Figure 6d,e. Only the UV-curable polymer substrate, bottom Au layer, CdS cavity layer, top Au layer, and water superstrate were taken into consideration for the calculation. As expected, by increasing the CdS layer thickness and decreasing the top Au thickness, the magnitude of the electric field stored in the cavity increases while the outcoupling to the superstrate also increases.

The significant increase in the field confinement and outcoupling to the superstrate with the increase in the cavity layer

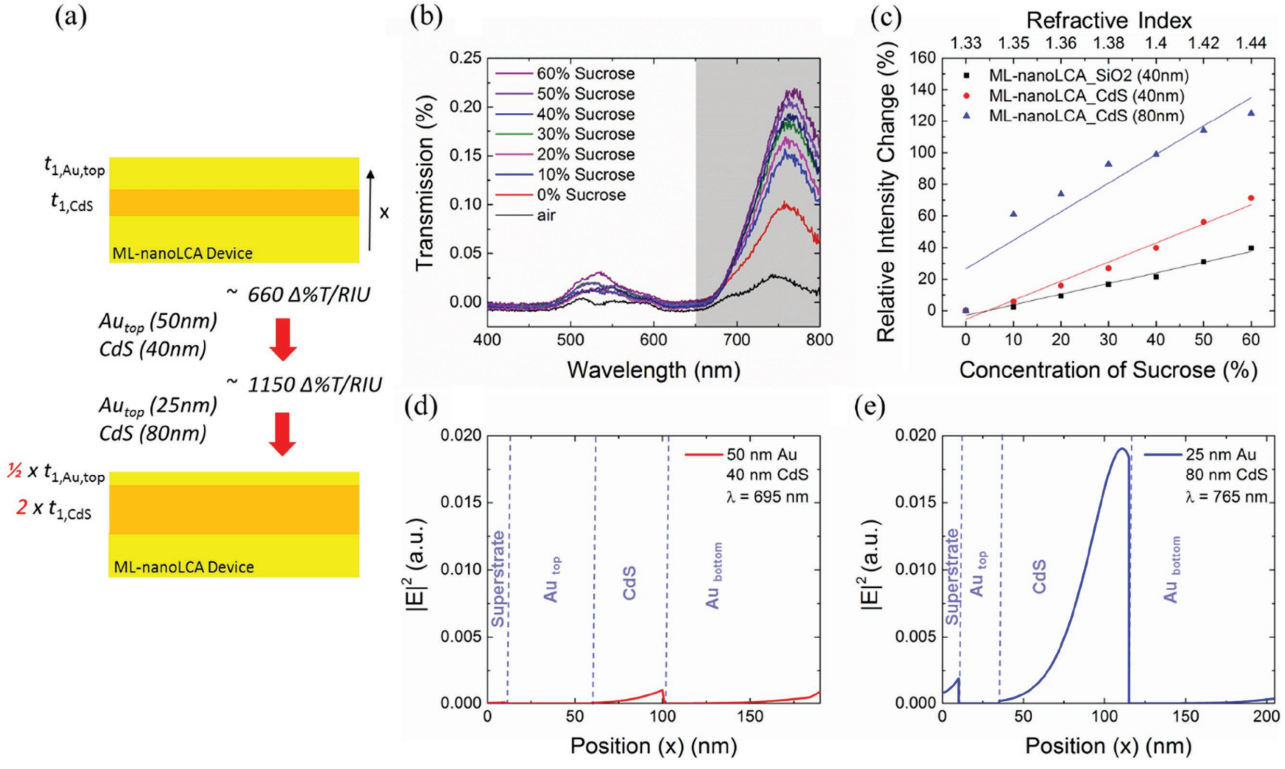

Figure 6. a) Schematic showing the changes made to the cavity structure and resulting increase in the sensitivity. b) Transmission spectra for the modified structure for increasing concentrations of sucrose (0%–60%) used for the sensitivity calculation. c) Graph comparing the measured relative intensity change of the ML-nanoLCA device for increasing concentrations of the sucrose solution and increasing RI with the modified cavity structure to the previous CdS and SiO_2 results. d) Electric field squared distribution for the case of a 50 nm top Au layer and 40 nm CdS layer. e) Electric field squared distribution for the case of a 25 nm top Au layer and 80 nm CdS layer.

© 2017 WILEY-VCH Verlag GmbH & Co. KGaA, Weinheim

thickness can be understood by considering the thickness required to obtain a cavity resonance. Assuming a simplified case of a Fabry–Perot cavity with a CdS dielectric surrounded by the two Au layers, the thickness of the CdS layer required to form a full cavity can be approximated. The full cavity will be obtained when there is constructive interference following a round trip in the cavity. Constructive interference occurs when the round trip phase, including the phase of the complex reflection coefficients of the CdS–Au interfaces, is equal to an integer multiplied by 2π. Following this condition (see the Supporting Information for derivation and Figure S4, Supporting Information), the cavity resonance is predicted to occur at 695 nm for a CdS layer thickness of 90 nm and the cavity resonance is predicted to occur at 765 nm for a CdS layer thickness of 105 nm. Therefore, for the 80 nm CdS cavity layer with a transmission peak at 765 nm, we are operating much closer to the cavity resonance and will have significantly higher field confinement in addition to a higher overall transmission compared to the 40 nm CdS cavity layer with a transmission peak at 695 nm. Note that if the resonance of the plasmonic sensor with no cavity structure and the cavity resonance were designed to be at the same wavelength, there would be a negligible change in the peak transmission when the RI of the superstrate changes because the peak transmission has a local maximum with respect to device geometry. Therefore, for greater sensitivity, we design the cavity to be slightly off resonance, for example, 80 nm instead of 105 nm for the CdS layer.

Additional electric field distributions, plotted using the transfer matrix method, for different cavity geometries are shown in Figure S5 (Supporting Information). These results also support that as the CdS cavity thickness is closer to the thickness required for a cavity resonance at a given wavelength, there will be both an increase in the electric field confined within the cavity layer and an increase in the electric field at the interface between the top Au layer and the superstrate. Further systematic study on the role of each layer in the multilayered stack including the influence of the relative thicknesses will be required to fully optimize the device for refractometric detection. Overall, the results presented in this work suggest that the sensing mechanism of the ML-nanoLCA is primarily driven by a change in transmission intensity that occurs due to a RI change on top of the nanostructured MIM cavity. This sensing mechanism also requires the plasmonic effect, which results in highly localized fields and induces strong light scattering.

3. Conclusion

This work has presented a new method for plasmonic RI sensing with significant improvements over current SPR systems. Unlike conventional SPR sensors, the ML-nanoLCA achieves RI sensing through the transmission peak intensity variation with no resonance peak shift; thus, a spectrometer that has high spectral resolution is not required. Due to the spectral features of this plasmonic nanocavity device, we anticipate that excitation and detection can be carried out using an LED and photodiode, respectively. However, further analysis on acceptable noise levels and signal integrity will need to be carried out to see if the same sensitivity and LOD can be maintained. The device also provides a greatly improved LOD (5×10^{-12} M for CEA) over typical EOT sensors and commercially available SPR systems and has a dynamic range in the concentrations relevant for human cancer biomarker detection. We studied the molecular binding kinetics on the ML-nanoLCA sensing surface with respect to time and calculated the important kinetic parameters (i.e., K_D). In this work, the sensitivity of the plasmonic nanocavity device was almost doubled by adjusting the thickness of the cavity layer. It is expected that further optimization of the coupling between the EOT plasmonic sensor and nanocavity will improve the LOD even further enabling highly sensitive, portable, and robust detections of biomolecular binding events.

4. Experimental Section

ML-NanoLCA Device Fabrication: The ML-nanoLCA device was fabricated using a replica molding process where the mold consists of a tapered nanopillar pattern made by laser interference lithography on a quartz substrate. UV-curable polymer (NOA-61, Sigma Aldrich) was evenly spread on the mold with a polyethylene terephthalate (PET) sheet backing on the top of it and exposed to UV light (105 mW cm^{-2}) for 2 min for curing. The PET substrate with the periodic nanohole pattern was carefully peeled off from the mold. In order to form the plasmonic device, a titanium (Ti) adhesion layer (9 nm) and an Au layer (90 nm) were deposited by e-beam evaporation. The CdS or SiO_2 cavity layer (40 or 80 nm) was then deposited using sputtering with an RF plasma. This was followed by e-beam evaporation of a 5 nm Ti adhesion layer and a top Au layer (50 or 25 nm) to form the nanocavity.

Spectral and Sensitivity Measurements: The transmission spectra through the ML-nanoLCA were measured by a Cary 5G UV–vis spectroscopy instrument in the wavelength range from 400 to 800 nm. The setup used a zero baseline correction in which the output spectrum was normalized with the light source of the system. The device sensitivity was measured in the unit of $\Delta\%T$/RIU as the relative change in the transmission (T) intensity at the wavelength that corresponds to the maximum intensity. To measure the sensitivity, sucrose solutions (Sigma-Aldrich) with different concentrations: 0%–60% mixed in Milli-Q water, which correspond to RI variation from 1.33 to 1.44, were added on the top of the ML-nanoLCA device and the transmission spectra were measured.

3D-FDTD Simulation for ML-NanoLCA: The 3D-FDTD simulation was performed using a commercial software package (Lumerical Solutions, Inc.). Periodic boundary conditions were imposed in *x*- and *y*-boundaries with a single nanocup modeled at the center of the FDTD region. The periodicity of the nanocup array was 320 nm. The cup was embedded in a dielectric material with the RI of 1.56, which is the RI of the NOA-61. The radius and the depth of the nanocup are 100 nm and 500 nm, respectively. The angle of the sidewall of the cup is 85° with respect to the *x*-axis. A continuous 9 nm Ti layer was then positioned along the surface of the dielectric followed by 90 nm Au, 40 nm CdS or SiO_2, and 90 nm Au layers. The material properties (RI and *k*) were taken from the *Handbook of Optical Constants of Solids*.[20] A 2 nm mesh was used, a plane wave was placed below the ML-nanoLCA structure with the propagation direction of +*z*, and a 1D monitor above the ML-nanoLCA structure was used for a transmission spectral calculation. 2D monitors in *xz*- and *yz*-planes were placed to obtain the electric field distributions. Perfectly matched layers were applied along the *z*-axis boundaries to avoid reflection and interference by the presence of the boundary.

DNA Hybridization: DNA-1 (5k thiol-GTT GTG TCC TGC TAA GTC CT), which is a ssDNA modified with a thiol group, was mixed with tris(2-carboxythyl)phosphine hydrochloride. The solution was incubated on the ML-nanoLCA surface at a concentration of 10×10^{-6} M for 16 h at 37 °C to break the S—S bond and immobilize the DNA-1 on the top Au surface. The device was then incubated in a blocking thiol solution MCH (6-mercapto-1-hexanol) at a concentration of 1×10^{-6} M for 1 h

© 2017 WILEY-VCH Verlag GmbH & Co. KGaA, Weinheim

at room temperature. For the final hybridization step, the ML-nanoLCA device was immersed in a 1×10^{-6} M DNA-2 (3′ complimentary base pair) solution for 16 h at 37 °C. Following each incubation step, the device was washed with Milli-Q water, dried with nitrogen (N_2), and the transmission spectrum was taken in water. (All materials were purchased from Sigma-Aldrich.)

Streptavidin–Biotin Binding: The ML-nanoLCA device was incubated in a 1×10^{-3} M solution of thiolated biotin at 37 °C followed by immersion in a 1×10^{-3} M MCH (6-mercapto-1-hexanol) blocking solution for 2 h at room temperature. In order to assess streptavidin binding to the immobilized biotin, the ML-nanoLCA device was immersed in a 1 μg mL^{-1} (18.9×10^{-9} M) streptavidin solution at room temperature. Following each incubation step, the device was washed with Milli-Q water, dried with nitrogen (N_2), and the transmission spectrum was taken in water. The binding of streptavidin was also monitored with respect to time by taking the transmission spectrum during the incubation. (All materials were purchased from Sigma-Aldrich.)

Transfer Matrix Method: The transfer matrix method was implemented in MATLAB (The MathWorks, Inc.) following a procedure for combining interface transitions and layer propagation in multilayered structures.[21] The backward propagation method was used and the result was normalized such that the incident intensity in all cases was the same. The RI for CdS was set to 2.5, the RI for the UV-curable polymer was set to 1.56, and the RI for the superstrate was set to 1.33. The RI and *k* for gold were taken from interpolated values from Johnson and Christy.[22]

CEA Detection: The devices were first incubated in a MUA solution in ethanol for 24 h at room temperature. The devices were then cleaned in 70% ethanol, dried in N_2, and the transmission spectra were taken in Milli-Q water. The devices were then dried in N_2 followed by incubation in a 1:1 mixture of 400×10^{-3} M EDC and 100×10^{-3} M NHS (both in Milli-Q water) at room temperature for 30 min. The devices were then rinsed in PBS and immediately incubated with 30 μg mL^{-1} monoclonal anti-CEA antibody at room temperature for 2 h. In the case of the antibody control, the device was incubated with 30 μg mL^{-1} mouse IgG for 2 h at room temperature. The sensors were then rinsed in PBS, dried with N_2, and the transmission spectra were taken in water. The sensors were then incubated for 30 min at room temperature in a 30 μg mL^{-1} BSA blocking solution followed by incubation for 30 min at room temperature in a 10% ethanolamine solution to cap the nonreacted NHS esters. The devices were then rinsed in Milli-Q water and the transmission spectra were taken in water. Finally, the devices were immersed in different concentrations of CEA for 2 h and the transmission spectra were taken in water in order to detect binding of CEA at the ML-nanoLCA surface. (All materials were purchased from Sigma-Aldrich.) Detection of CEA was also carried out in human serum samples. Devices were functionalized as described previously, but for the final incubation 1 μg mL^{-1} and 100 ng mL^{-1} of CEA were spiked in human blood serum samples (Zen-Bio) and incubation was done for 2 h before cleaning in Milli-Q water and taking the transmission spectra in water.

Supporting Information

Supporting Information is available from the Wiley Online Library or from the author.

Acknowledgements

A.A., L.P.H., and S.S. contributed equally to this work. This work was funded by the U.S. Department of Agriculture Award No. 2014-06959. Funding for L.P.H. was provided by the Linda Su-Nan Chang Sah doctoral fellowship. The authors thank Numair Ahmed for the schematic diagram. The authors also thank Hoang Nguyen, Cindy Larson, and Tiziana Bond of Lawrence Livermore National Laboratory for preparation of the master nanopillar mold. The authors also thank Micro Nanotechnology Laboratory and Frederick Seitz Materials Research Laboratory Central Facilities for providing research facilities.

Keywords

carcinoembryonic antigens, extraordinary optical transmission, nanohole array sensors, nanostructure fabrication, surface plasmon resonance

Received: December 12, 2016
Revised: February 17, 2017
Published online:

[1] Y. B. Guo, J. Y. Ye, C. Divin, B. H. Huang, T. P. Thomas, J. R. Baker, T. B. Norris, *Anal. Chem.* **2010**, *82*, 5211.
[2] M. Iqbal, M. A. Gleeson, B. Spaugh, F. Tybor, W. G. Gunn, M. Hochberg, T. Baehr-Jones, R. C. Bailey, L. C. Gunn, *IEEE J. Sel. Top. Quantum Electron.* **2010**, *16*, 654.
[3] V. S. Y. Lin, K. Motesharei, K. P. S. Dancil, M. J. Sailor, M. R. Ghadiri, *Science* **1997**, *278*, 840.
[4] B. Liedberg, C. Nylander, I. Lundstrom, *Sens. Actuators* **1983**, *4*, 299.
[5] I. E. Tothill, *Sem. Cell Dev. Biol.* **2009**, *20*, 55.
[6] a) A. G. Brolo, R. Gordon, B. Leathem, K. L. Kavanagh, *Langmuir* **2004**, *20*, 4813; b) T. W. Ebbesen, H. J. Lezec, H. F. Ghaemi, T. Thio, P. A. Wolff, *Nature* **1998**, *391*, 667.
[7] a) V. Canalejas-Tejero, S. Herranz, A. Bellingham, M. C. Moreno-Bondi, C. A. Barrios, *ACS Appl. Mater. Interfaces* **2014**, *6*, 1005; b) J. C. Sharpe, J. S. Mitchell, L. Lin, N. Sedoglavich, R. J. Blaikie, *Anal. Chem.* **2008**, *80*, 2244.
[8] a) R. Zia, M. D. Selker, P. B. Catrysse, M. L. Brongersma, *J. Opt. Soc. Am. A* **2004**, *21*, 2442; b) H. Choo, M. K. Kim, M. Staffaroni, T. J. Seok, J. Bokor, S. Cabrini, P. J. Schuck, M. C. Wu, E. Yablonovitch, *Nat. Photonics* **2012**, *6*, 837; c) V. E. Babicheva, R. Malureanu, A. V. Lavrinenko, *Photonics Nanostruct.* **2013**, *11*, 323; d) A. Hosseini, Y. Massoud, *J. Opt. Soc. Am. A* **2007**, *24*, 221.
[9] a) Y. F. Liu, J. Kim, *Sens. Actuators, B* **2010**, *148*, 23; b) A. Syahir, K. Kajikawa, H. Mihara, *Chem. Asian J.* **2012**, *7*, 1867.
[10] a) H. L. Duan, Y. M. Xuan, *Physica E* **2011**, *43*, 1475; b) C. Wadell, T. J. Antosiewicz, C. Langhammer, *Nano Lett.* **2012**, *12*, 4784.
[11] a) D. Chanda, K. Shigeta, T. Truong, E. Lui, A. Mihi, M. Schulmerich, P. V. Braun, R. Bhargava, J. A. Rogers, *Nat. Commun.* **2011**, *2*, 479; b) T. Cao, C. Wei, L. Zhang, *Opt. Mater. Express* **2014**, *4*, 1526; c) J. Junesch, T. Sannomiya, A. B. Dahlin, *ACS Nano* **2012**, *6*, 10405; d) A. B. Dahlin, M. Mapar, K. L. Xiong, F. Mazzotta, F. Hook, T. Sannomiya, *Adv. Opt. Mater.* **2014**, *2*, 556; e) M. Tabatabaei, M. Najiminaini, K. Davieau, B. Kaminska, M. R. Singh, J. J. L. Carson, F. Lagugne-Labarthet, *ACS Photonics* **2015**, *2*, 752.
[12] a) M. R. Gartia, A. Hsiao, A. Pokhriyal, S. Seo, G. Kulsharova, B. T. Cunningham, T. C. Bond, G. L. Liu, *Adv. Opt. Mater.* **2013**, *1*, 68; b) T. W. Chang, X. H. Wang, A. Hsiao, Z. D. Xu, G. H. Lin, M. R. Gartia, X. R. Liu, G. L. Liu, *Adv. Opt. Mater.* **2015**, *3*, 1397; c) A. Hsiao, M. R. Gartia, T. W. Chang, X. Wang, P. Khumwan, G. L. Liu, *Sens. Bio-Sens. Res.* **2015**, *5*, 24; d) L. Plucinski, M. R. Gartia, W. R. Arnold, A. Ameen, T. W. Chang, A. Hsiao, G. L. Liu, A. Das, *Biosens. Bioelectron.* **2016**, *75*, 337; e) S. Seo, A. Ameen, G. L. Liu, *J. Phys. Chem. C* **2015**, *119*, 18518.
[13] a) A. P. Blanchard-Dionne, L. Guyot, S. Patskovsky, R. Gordon, M. Meunier, *Opt. Express* **2011**, *19*, 15041; b) M. E. Stewart, N. H. Mack, V. Malyarchuk, J. A. N. T. Soares, T. W. Lee, S. K. Gray, R. G. Nuzzo, J. A. Rogers, *Proc. Natl. Acad. Sci. USA* **2006**, *103*, 17143.
[14] J. S. Macdonald, *Semin. Oncol.* **1999**, *26*, 556.

 © 2017 WILEY-VCH Verlag GmbH & Co. KGaA, Weinheim

[15] L. Hernandez, A. Espasa, C. Fernandez, A. Candela, C. Martin, S. Romero, *Lung Cancer* **2002**, *36*, 83.
[16] M. J. Duffy, A. van Dalen, C. Haglund, L. Hansson, R. Klapdor, R. Lamerz, O. Nilsson, C. Sturgeon, O. Topolcan, *Eur. J. Cancer* **2003**, *39*, 718.
[17] a) K. Bremer, S. Micus, G. Bremer, *Eur. J. Cancer* **1995**, *31*, S262; b) R. Molina, J. Jo, X. Filella, G. Zanon, J. Pahisa, M. Munoz, B. Farrus, M. L. Latre, C. Escriche, J. Estape, A. M. Ballesta, *Breast Cancer Res. Treat.* **1998**, *51*, 109.
[18] Z. Altintas, Y. Uludag, Y. Gurbuz, I. E. Tothill, *Talanta* **2011**, *86*, 377.
[19] a) H. J. Lee, A. W. Wark, T. T. Goodrich, S. P. Fang, R. M. Corn, *Langmuir* **2005**, *21*, 4050; b) K. S. Phillips, Q. Cheng, *Anal. Bioanal. Chem.* **2007**, *387*, 1831.
[20] E. D. Palik, G. Ghosh, *Handbook of Optical Constants of Solids*, Academic Press, San Diego, CA **1998**.
[21] S. L. Chuang, *Physics of Photonic Devices*, Wiley, Hoboken, NJ **2009**.
[22] P. B. Johnson, R. W. Christy, *Phys. Rev. B* **1972**, *6*, 4370.

 © 2017 WILEY-VCH Verlag GmbH & Co. KGaA, Weinheim